Microfluidics of the Decomposition of Hydrogen Peroxide in MEMS Microthrusters

Paolo Tortora

ALMA MATER STUDIORUM UNIVERSITA' DI BOLOGNA SEDE

05/23/2017
Final Report

<div style="text-align:center">

REPORT DOCUMENTATION PAGE

Form Approved
OMB No. 0704-0188

</div>

1. REPORT DATE *(DD-MM-YYYY)*	2. REPORT TYPE	3. DATES COVERED *(From - To)*
24-05-2017	Final	01 Dec 2015 to 30 Nov 2016

4. TITLE AND SUBTITLE
Investigation on the Physics and Microfluidics of the Decomposition of Hydrogen Peroxide in MEMS Microthrusters

5a. CONTRACT NUMBER

5b. GRANT NUMBER
FA9550-16-1-0081

5c. PROGRAM ELEMENT NUMBER
61102F

6. AUTHOR(S)
Paolo Tortora

5d. PROJECT NUMBER

5e. TASK NUMBER

5f. WORK UNIT NUMBER

7. PERFORMING ORGANIZATION NAME(S) AND ADDRESS(ES)
ALMA MATER STUDIORUM UNIVERSITA' DI BOLOGNA SEDE
VIA ZAMBONI 33
BOLOGNA, 40126 IT

8. PERFORMING ORGANIZATION REPORT NUMBER

9. SPONSORING/MONITORING AGENCY NAME(S) AND ADDRESS(ES)
EOARD
Unit 4515
APO AE 09421-4515

10. SPONSOR/MONITOR'S ACRONYM(S)
AFRL/AFOSR IOE

11. SPONSOR/MONITOR'S REPORT NUMBER(S)
AFRL-AFOSR-UK-TR-2017-0034

12. DISTRIBUTION/AVAILABILITY STATEMENT
A DISTRIBUTION UNLIMITED: PB Public Release

13. SUPPLEMENTARY NOTES

14. ABSTRACT
We performed a numerical investigation of the microfluidics within peroxide monopropellant microthrusters. One of the challenges with microscale thrusters is that, as the size is reduced, the ratio of the surface area to volume increases. Therefore, the heat losses (surface phenomenon) become significant compared to the heat generated by the exothermic reaction within the device (volume phenomenon), and the thermal energy available inside the combustion chamber may not be sufficient for sustaining the reaction and vaporization of the liquid products and non-reacted propellant. To gain more insight over the complex interactions within the combustion chamber, we developed a numerical model which jointly analyzes the chemical, fluid-dynamics and thermal behavior of the propellant stream inside the combustion chamber, as well as the thermal coupling with a conductive substrate. Within this model, evaporation is handled by making use of a variable heat capacity method and the concept of pseudo-phase. This method offers a sound way to model the evaporation in a chemical reacting mixture. As a main result, it emerged that the substrate has a great impact on the flow evolution, with an evaporation region distributed all over the length of the device, affecting also the propellant conversion rate.

15. SUBJECT TERMS
EOARD, microthruster, MEMS propulsion, microfluidics, hydrogen peroxide, monopropellant

16. SECURITY CLASSIFICATION OF:			17. LIMITATION OF ABSTRACT	18. NUMBER OF PAGES	19a. NAME OF RESPONSIBLE PERSON
a. REPORT	b. ABSTRACT	c. THIS PAGE			MILLER, KENT
Unclassified	Unclassified	Unclassified	SAR	39	**19b. TELEPHONE NUMBER** *(Include area code)* 011-44-1895-616022

Investigation on the physics and microfluidics of the decomposition of H2O2 in MEMS µ-thrusters

Prepared by:	Paolo Tortora, Dario Modenini, Alberto Lucci
Release date:	28th February 2017

This page is intentionally left blank

TABLE OF CONTENTS

		Version	1.0
	Final Report	**Date**	28/02/2017

1. LIST OF FIGURES
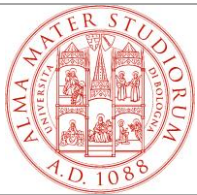
	Final Report	**Version**	**1.0**
		Date	**28/02/2017**

2. LIST OF TABLES

DISTRIBUTION A. Approved for public release: distribution unlimited.

3. SUMMARY

This report summarizes the results of the study undertaken by the authors under USAF Grant n° FA9550-16-1-0081.

The work performed lies within the context of a wider collaboration agreement undertaken jointly by UniBo team with a private company and a research institute, towards the development of a MEMS prototype of a hydrogen peroxide microthruster delivering thrust in the mN range, and targeting the class of micro-nano spacecraft.

Most of the work consisted in theoretical and numerical analysis of the flow within the dissociation chamber. This is deemed to be an important tool to guide the design phase of the microthrusters.

The report is structured as follow:

- Introduction and motivation for the investigation.
- Development of the numerical model, including detailed discussion of the mathematical framework and analysis of the results.
- Design activities in preparation of the manufacturing of the next thrusters prototypes.
- Conlcusions.

4. REFERENCES

Ref	Title
[1]	S. J. Widdis, K. Asante, D. L. Hitt, M. W. Cross, W. J. Varhue, R. McDevitt, "A MEMS-Based Catalytic for H_2O_2 Monopropellant Micropropulsion System" (2013)
[2]	R. McDevitt, D. L. Hitt, "Numerical Study of Liquid Phase Hydrogen Peroxide Decomposition in Catalytic Micro-Reactor, Proceedings of the International Conference on New Trends in Transport Phenomena, May 2014
[3]	E. Lennon, A.A. Burkeb, M. Ocampo, R.S. Bessera, "Microscale packed bed reactor for controlled hydrogen peroxide decomposition as a fuel cell oxidant aboard unmanned undersea vehicles", Journal of Power Sources, 195 (2010) 299–306.
[4]	S. Bonifacio and A. Russo, "Modeling hydrogen peroxide decomposition in monolithic beds," in Proc. 3rd Int. Conf. Green Propellant Space Propuls., 9th Int. Hydrogen Peroxide Propuls. Conf. ESA SP-635 (2006), pp. 1–6
[5]	Koopmans, R. J. "Modelling of Multiphase Multicomponent Chemically Reacting Flows through Packed Beds", PhD Dissertation, University of Southampton (2013)
[6]	Kee, J. R. Coltrin, M. E. Glarborg, P "Chemically reacting flow: theory and practice", John Wiley & Sons (2003)
[7]	Haider - Numerical Modelling of Evaporation and Condensation Phenomena - Master Thesis, University of Stuttgart (2013)

5. ACRONYMS

Abbreviation	Meaning
CFD	Computational Fluid Dynamics
FEM	Finite Element Method
HTP	High Test Peroxide
MEMS	Micro electro-mechanical systems
PVD	Physical Vapor Deposition
UniBO	University of Bologna

DISTRIBUTION A. Approved for public release: distribution unlimited.

6. INTRODUCTION

Many Space Agencies are currently pursuing the development of light, small S/C platforms for a wide range of missions (such as Earth observation and formation flying), and a major critical point is indeed represented by the on-board propulsion technologies to meet the orbit correction/control and de-orbiting needs. The typical ΔV values needed by such missions are incompatible with simple cold-gas systems but, at the same time, the toxicity hazards placed by hydrazine or the often-prohibitive power needs of electrical propulsion calls for the search of alternative propellant solutions. A very promising technology is represented by hydrogen peroxide based monopropellant systems, which offers the highest volumetric specific impulse, as compared to many other propellants.

Propulsion systems in which the release of thermal energy is obtained through a catalytic decomposition, need a propellant only and, for this reason, are usually called "monopropellant thrusters".

Due to its reduced toxicity, the nature of the decomposition products and environmental friendless, hydrogen peroxide has gained increased attention. In micro/nano spacecraft applications where cost reductions are being emphasized, eased procurement and handling procedures that such a propellant yield, feature prominently. On top of that, a great asset in miniaturization may come from a MEMS-based thruster manufacturing process, which has been already exploited in the past years for cold-gas micro-propulsion.

6.1 Motivations

One of the challenges with microscale thrusters is that, as the size is reduced, the ratio of the surface area to volume increases. Therefore, the heat losses (surface phenomenon) become significant compared to the heat generated by the exothermic reaction within the device (voume phenomenon), and the thermal energy available inside the combustion chamber may not be sufficient for sustaining the reaction and vaporization of the liquid products and/or non-reacted peroxide. The effects of boundary layers also become more pronounced at small scales and can lead to significant deviations from inviscid behavior.

For similar reasons, MEMS-based devices are well suited to host heterogeneous catalytic processes, which are surface reactions, due to their intrinsically high surface to volume ratio. However, the lack of sound understanding of the coupling between heterogeneous catalysis, multiphase fluid dynamics, and thermal phenomena makes it a difficult task to estimate the critical length needed to obtain a complete propellant decomposition, based on simple considerations only.

An empirical approach would be the one which scales the literature data available for larger HTP thrusters down to the MEMS size. This exercise results in an estimated length of ≈ 2 mm. At this small scales the Reynolds number is very low leading to laminar flow regardless of the geometry and therefore very little mixing occurs. In other words, diffusion and conduction are the dominant modes of species and heat transport. This in turn suggests that direct application of downscaling is questionable, since in large scale devices turbulent mixing occur. It is therefore reasonable to expect the former exercise to lead to a considerable underestimation of the critical length.

The critical channel length must be selected such that, for a given mass flow rate, complete decomposition occurs. If the chamber is too short, incomplete decomposition will result in diminished efficiency. If the channel is too long condensation may occur.

DISTRIBUTION A. Approved for public release: distribution unlimited.

Given the discussion above, the design of the thrusters object of this study cannot be based solely on semi-empirical arguments rather, a comprehensive numerical analysis is required.

6.2 Background

The background activity undertaken by the team as a joint collaboration agreement, lead to a first design of microthruster a few years ago: this design forms the baseline for the next generation also. The first prototypes of H_2O_2 micro-thrusters, manufactured at an external research institute premises, were silicon MEMS devices featuring a decomposition chamber configured as a dense pattern of staggered pillars. The great number of pillars was aimed at maximizing the catalyst surface per unit volume to enhance the decomposition. The overall dimensions of those prototypes were approximately $18\times4\times1mm^3$.
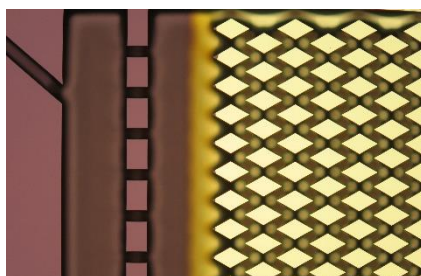
Figure 6-1: Staggered pillar concept for the decomposition chamber.

Experimental testing of those samples showed however an insufficient propellant conversion, with a bubbly gas-liquid mixture found at the outlet. These results called for a more in depth investigation of the underlying physics, to provide some guidelines for the design.

For the numerical analysis performed during this study, the staggered-pillars layout was retained: indeed, as a result of the design optimization we expect to tailor the size, spacing, shape of pillars, without changing dramatically the overall concept.

7. NUMERICAL MODEL

7.1 Literature Review

The design of a reliable high test peroxide based monopropellant systems is strictly related to our capacity of developing a numerical model capable of simulating the heterogeneous catalytic decomposition process of liquid hydrogen peroxide.

The exothermic reaction at the base of the operation of the device evolves as a sequence of the three following stages:

1. A first stage where both peroxide and water exist in the liquid phase;
2. A second stage where the aqueous peroxide mixture is boiling;
3. A third and final stage where both are in the gas phase.

In all three stages, peroxide and water coexist with gaseous oxygen.

It is evident as a full simulation of the decomposition reaction is extremely challenging and complicated by the multiphase nature of the flow and by the coupling of heat and mass transfer.

There is a quite extensive literature on numerical modelling for the decomposition of hydrogen peroxide in thrusters and/or micro-reactors in general. As a matter of fact, this topic cannot yet be considered fully covered, since, whether to a smaller or to a greater extent, some simplifying assumptions shall be made if one wants to develop a tractable/solvable numerical model.

A common simplified approach is the one which models one single phase at a time. For example, in [1] the decomposition of the vapor phase was considered in a 2D model of a microreactor, with the chemical reactions modelled using a simplified formulation with one species concentration equation (typically used for dilute solutions), and no interaction with the solid domain considered.

Alternatively, it is possible to consider what happens in a pre-vaporization condition to evaluate the effect of the monopropellant in its liquid form and the heat generation associated with the decomposition, as done in [2] , where the interaction with the substrate was still absent.

In [3] , a 3D simulation for the decomposition of a 50% aqueous peroxide solution within a packed bed microreactor is presented, where evaporation is partially accounted for, but only for the water species. Again, the species conservation was implemented with a simplified single equation for molar concentration.

Numerical models which encompasses all the phases have been developed in the past, but are limited to 1D studies, as in [4] , [5] .

As a natural complement to the work performed in the cited references, in the present study we sought for a unique model capable of modelling the decomposition process both in the pre- and post-vaporization phases of the liquid reactants and products.

7.2 Development of an evaporation model for the decomposition of H_2O_2 suitable for FEM analysis

The literature review showed that three main aspects are overlooked in the models developed so far:

1- A sound treatment of the chemical species conservation, usually relegated to a single species equation, more suited for diluted solutions.
2- A theoretical model which jointly accounts for the dissociation of the propellant and its evaporation due to the temperature increase, to be integrated in the overall FEM model.
3- Effect of the conjugate thermal problem of the fluid stream and the silicon substrate.

This last point is of great importance due to the high thermal conductivity of the silicon substrate, which enhances the transport of the generated heat of reaction all along the chamber length. It is worth to be noted that to capture all the relevant phenomena, especially point 3, a 3D model is required.

To this end, a commercial FEM code was employed (COMSOL Multiphysics) which allows the coupling of several physical interfaces. The global numerical model can then be thought as the sum of several PDE solved within the two domains, fluid and solid, according to the following:

a) FLUID
   1. Species transport
   2. Mixture continuity
   3. Momentum transport
   4. Energy transport (including phase change)
b) SOLID
   1. Energy transport

DISTRIBUTION A. Approved for public release: distribution unlimited.

To limit the computational burden, the geometric domain is restricted to only one *elementary slit* (see Figure 7-1) of the combustion chamber, without detailed modelling of the inlet and outlet regions. This simplification retains nevertheless the fundamental structure of the current design for the combustion chamber, implemented as a dense pattern of staggered pillars. Main geometric dimensions are collected in Table 7-1.

The mesh is composed by slightly more than 1 million of elements, prism in the fluid domain and tetrahedral in the solid domain. As apparent from Figure 7-2, a finer mesh was set up for the fluid domain, while a much coarser discretization was chosen for the silicon substrate.

Due to the chosen approach of modeling only an elementary slit, an extensive use has been made of the "symmetric boundary" feature, which is common to many CFD software for exploiting the planes of symmetry of the geometry under study. By referring to Figure 7-1, the symmetry planes are the two lateral x-z sides, plus the top side, x-y, since only one-half of the channel height is modelled.

Description	Size [m]
Length	9e-3
Width	1e-4
Height	2e-4[1]
Substrate thickness	4e-4
Pillar size (l_x)[2]	2.6e-4
Pillar size (l_y)	0.75e-4
Pillar spacing (Δx)	1e-4
Pillar spacing (Δy)	0.25e-4

Table 7-1: Summary of the main dimensions for the baseline geometrical model.
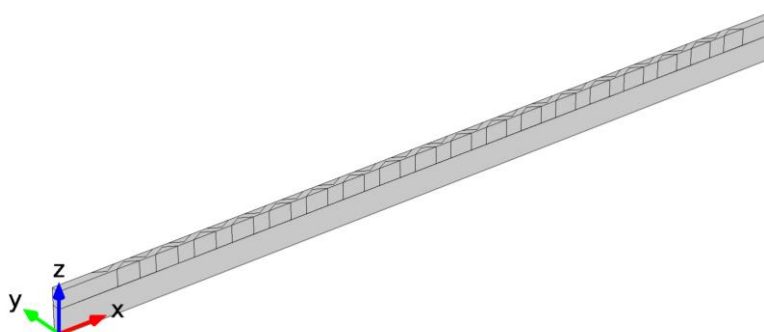
Figure 7-1: Isometric view of a domain modelled with equispaced, diamond pillars

---

[1] Half-heigth of the fluid domain (simmetry condition)
[2] Length of rhombus diagonals.

DISTRIBUTION A. Approved for public release: distribution unlimited.
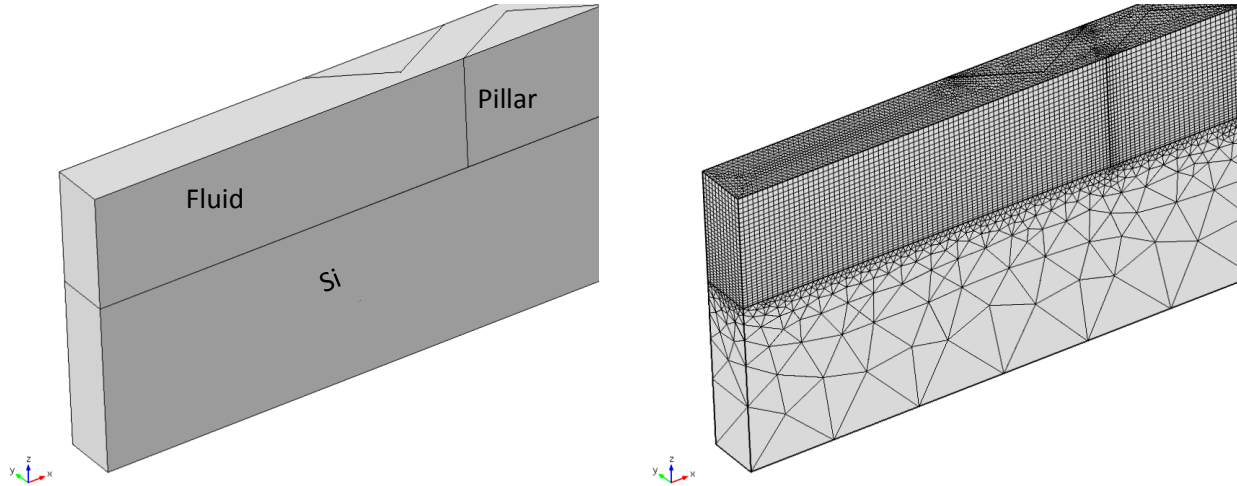
Figure 7-2: Detailed view of the inlet region: geometry (left) and mesh (right)

7.3 Fluid domain

The mathematical model for the chemically reacting flow dynamics is adapted from [6] , where conservation equations are formulated for the species mass fractions.

7.3.1 Species transport

Transport of chemical species is subjected to the following equation for the mass fraction Y_k, describing the conservation of mass:

$$\rho \frac{DY_k}{Dt} = -\boldsymbol{\nabla} \cdot \mathbf{j}_k + \dot{r}_k MM_k \tag{7-1}$$

where $\mathbf{j}_k$ is the diffusive mass flux and $\frac{D}{Dt} = \frac{\partial}{\partial t} + \mathbf{u} \cdot \boldsymbol{\nabla}$ stands for substantial derivative.

There exist several theories for describing multi-component diffusion. Here we have chosen a mixture-averaged formulation, which is not the most rigorous implementation, still it is sufficient for our purpose, which is to perform an "order-of-magnitude" evaluation of the impact of diffusion coefficients over the combustion chamber efficiency. In such formulation, the diffusive flux reads as:

$$\mathbf{j}_k = \rho D_k^m \left(\boldsymbol{\nabla} Y_k + \frac{Y_k}{\overline{MM}} \nabla \overline{MM} \right) \tag{7-2}$$

where $\overline{MM}$ and D_k^m are, respectively the *mixture-averaged molar mass* and *mixture-averaged diffusion coefficient* for species k[3]. Note that, to ensure total mass conservation, the equation above is solved for 2 species only, and the mass fraction of the third one is computed as the complement to 1. In the simulations performed, the specie solved for through mass conservation is H_2O_2.

Note that ρ is the *average mixture density*, and it will be better defined when describing the energy transport equation and the evaporation model.

---

[3] Full expressions for $\overline{MM}$ and D_k^m can be found, e.g. in [6] .

Summing up the contribution of the different species leads to the standard continuity equation for single-phase, non-reacting fluid, since the sum of all diffuses fluxes as well as all reaction rates must be zero by definition:

$$\frac{D\rho}{Dt} = 0 \qquad (7\text{-}3)$$

7.3.2 Momentum transport

The momentum transport is described by the well-known Navier-Stokes equation:

$$\rho \frac{D\mathbf{u}}{Dt} = \nabla \cdot \left[-p\boldsymbol{I} + \mu(\nabla\mathbf{u} + \nabla\mathbf{u}^T) - \frac{2}{3}\mu(\nabla \cdot \mathbf{u})\boldsymbol{I} \right] \qquad (7\text{-}4)$$

Where **u** is the velocity field, p the pressure field and μ the dynamic viscosity of the mixture. This implementation relies on the assumption of low-Mach number flow, which is certainly satisfied within the combustion chamber.

7.3.3 Energy transport

The equation for the transport of enthalpy (on a *mass* basis, i.e. [J/kg]) in a homogeneous chemically reacting flow reads as:

$$\rho \frac{DH}{Dt} = \frac{Dp}{Dt} + \boldsymbol{\nabla} \cdot (\kappa\nabla T) - \sum_{k=1}^{K} \boldsymbol{\nabla} \cdot (H_k \cdot \mathbf{j}_k) + \Phi \qquad (7\text{-}5)$$

It highlights the various mechanisms for enthalpy transport, i.e. pressure work, Dp/Dt, thermal conduction $\nabla \cdot (\kappa\boldsymbol{\nabla}T)$, enthalpy variation due to diffusive transport of species $\sum_{k=1}^{K} \boldsymbol{\nabla} \cdot (H_k \cdot \mathbf{j}_k)$, and viscous dissipation Φ (whose explicit expression may be found in standard textbooks). In the present application, (low pressure, low velocity flow) the viscous dissipation and pressure work terms can be safely neglected. Furthermore, it is often convenient to express the enthalpy transport equation in terms of temperature only, which leads to:

$$\rho c_p \frac{DT}{Dt} = \frac{Dp}{Dt} + \boldsymbol{\nabla} \cdot (\kappa\nabla T) - \sum_{k=1}^{K} c_{p,k}\mathbf{j}_k \cdot (\kappa\nabla T) - \sum_{k=1}^{K} H_k \dot{r}_k M_k + \Phi \qquad (7\text{-}6)$$

In general, for a gaseous mixture, the mixture averaged properties are evaluated as:

$$c_p = \sum_{k=1}^{K} c_{p,k} Y_k ; \quad H = \sum_{k=1}^{K} H_k Y_k ; \quad \rho = \frac{1}{\sum_{k=1}^{K} \frac{Y_k}{\rho_k}} \qquad (7\text{-}7)$$

I.e. the specific heat and enthalpy are weighted averages of the respective species coefficient weighted through mass fractions, while the density is a weighted average of the volume fractions. Later, these expressions will be generalized to account for the phase change.

The enthalpy of each species has been assumed independent on the pressure (strictly true for perfect gases, approximately true for real gases and liquids at low pressure):

$$dH_k = c_{p,k}dT$$

The temperature formulation brings also naturally out the concept of enthalpy of reaction, through the introduction of the source term $\sum_{k=1}^{K} H_k \dot{r}_k MM_k$ which depends on the reaction rate $\dot{r}_k$ [mol/m³s].

Note that the expression for the mixture density is in accordance with the usual volume fraction formulation for immiscible fluids, as it is the case when dealing with different phases.

For the case under study, where the catalytic dissociation of hydrogen peroxide occurs at the catalytic surface, the enthalpy of reaction enters the system as a boundary heat flux rather than a volumetric source (and its dimensions change to [mol/(m²s)] accordingly).

This formulation, although general, does not directly accommodate phase changing fluids. However, the vaporization process can be handled thanks to a technique that is known in the literature as the "*equivalent heat capacity method*", originally conceived for melting solids, and further developed in this framework to the problem at hand.

Essentially this method rather than employing the common *latent heat of vaporization L_{vap}* as an additive term in the energy balance equation when a material reaches its phase change temperature T_{pc}, prescribes that the phase change occurs in a *temperature interval* between $T_{pc} - \Delta T/2$ and $T_{pc} + \Delta T/2$. In this interval, the following assumptions are made:

1. A smooth function of temperature, θ, is defined, which is equal to 1 before $T_{pc} - \Delta T/2$ and to 0 after $T_{pc} + \Delta T/2$. It corresponds to the volume fraction of phase 1 within the mixture

2. The density, ρ, and the specific enthalpy, H [J/kg] of the mixture are expressed as a *convex combination* of the respective values for the *phase 1* (before evaporation starts) and *phase 2* (fully evaporated mixture).

Assumption 2 results into the following equations:

$$\rho = \theta\rho_1 + (1-\theta)\rho_2 \tag{7-8}$$

$$\rho H = \theta\rho_1 H_1 + (1-\theta)\rho_2 H_2 \tag{7-9}$$

The same combination is also used for computing the mixture viscosity μ, necessary for solving momentum transport:

$$\mu = \theta\mu_1 + (1-\theta)\mu_2 \tag{7-10}$$

Note that mass and species convervation are ensured by using the expression in Eq. (7-8) for the density used to solve both Eq. (7-1) and (7-3).

Therefore, the method basically provides a constitutive equation for the variation of the volume fraction within the evaporating mixture as a function of temperature only. Note that, however, a dependency on the chemical composition is still retained, since the physical properties of the two states, 1 and 2, at the beginning and end of the evaporation interval, are indeed functions of the local composition through Eqs. (7-7): depending on the inlet propellant concentration, and boundary conditions, we may expect that the $T_{pc} - \Delta T/2$ and $T_{pc} + \Delta T/2$ temperature levels may be reached at different degree of propellant dissociation, and this is fully accounted for in the definition of states 1 and 2.

Differentiating the enthalpy w.r.t. temperature to find the specific heat capacity, we have:

$$
\begin{aligned}
c_p &= \frac{\partial}{\partial T}\left(\frac{\theta \rho_1 H_1 + (1-\theta)\rho_2 H_2}{\rho}\right) \\
&= \frac{1}{\rho}\left[(\theta \rho_1 c_{p,1} + (1-\theta)\rho_2 c_{p,2}) + \frac{\partial \theta}{\partial T}\left(\rho_1 H_1 - \rho_2 H_2 - \frac{\rho_1 - \rho_2}{\rho}(\rho H)\right)\right] \qquad (7\text{-}11)\\
&= \frac{1}{\rho}\left[(\theta \rho_1 c_{p,1} + (1-\theta)\rho_2 c_{p,2}) + \frac{\partial \theta}{\partial T}\left(\rho_1(H_1 - H) - \rho_2(H_2 - H)\right)\right]
\end{aligned}
$$

Which is composed by a first term, i.e. a volume averaged *specific heat coefficients*, and a second term, proportional to the assumed $\frac{\partial \theta}{\partial T}$, which depends on the difference between the enthalpies of the two phases, H_1 and H_2. This last can be interpreted as the *enthalpy of vaporization* which is originated by the different enthalpies of formation between the liquid and vapor phases and is distributed over the entire temperature range.

The specific enthalpies for the two phases are computed as:

$$H_1 = H_{O_2}Y_{O_2} + H_{H_2O_2(l)}Y_{H_2O_2} + H_{H_2O(l)}Y_{H_2O}$$

$$H_2 = H_{O_2}Y_{O_2} + H_{H_2O_2(v)}Y_{H_2O_2} + H_{H_2O(v)}Y_{H_2O}$$

Where $H_i = H_i^o + \int_{T^o}^{T} c_{p,i} dT$

The boiling point is in principle a function of the concentration of the saturated liquid, ranging from 100°C (pure water) to 150°C (pure peroxide), see Figure 7-3. Therefore, one may expect the boiling, within the chemically reacting stream with variable composition, to be a continuous process inside this interval: this is the pivoting assumption in our method, which yields to T_{pc} = 125°C and ΔT = 50°C.
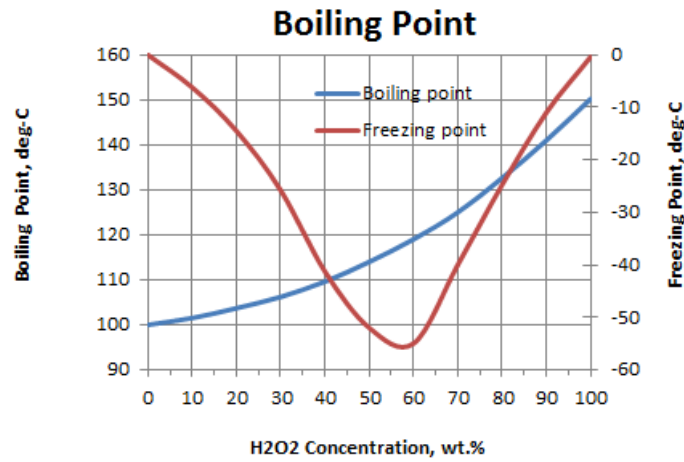
Boiling Point

Figure 7-3: Plots of Boiling and freezing points of hydrogen peroxide aqueous solutions as a function of weight fraction

In our case, we should better talk of pseudo-phases since, actually, what we can identify as "phase 1" is rather a combination of liquid H_2O_2-H_2O mixture and gaseous O_2. Phase 2 is a fully gaseous mixture (O_2 plus H_2O_2-H_2O vapors) which is treated as a perfect gas.

The density of phase-1 is computed in the assumption of immiscible fluids sharing the same velocity field as:

$$\rho_1 = \frac{1}{\frac{Y_l}{\rho_l} + \frac{Y_{O_2}}{\rho_{O_2}}} \qquad (7\text{-}12)$$

Where ρ_l is the density of the liquid H_2O_2-H_2O mixture, known through fitting functions of the temperature and wt% available from literature, and the oxygen density is computed as: $\rho_{O_2} = \frac{MM_{O_2}p}{RT}$.

As concerning density of phase 2, from ideal gas law $\rho_g = \frac{MM_g p}{RT}$, with the mixture molar mass MM_g defined as:

$$MM_{mix} = \frac{1}{\left(\frac{Y_p}{MM_p} + \frac{Y_w}{MM_w} + \frac{Y_{O_2}}{MM_{O_2}}\right)} \qquad (7\text{-}13)$$

7.3.4 Reaction kinetics

Reaction kinetics has been assumed *first order* in the molar concentration C_{H2O2} [mol/m₃]:

$$\dot{r}_{H_2O_2} = -k'' \cdot C_{H_2O_2} \quad \dot{r}_{H_2O} = -\dot{r}_{H_2O_2} \quad \dot{r}_{O_2} = -\frac{1}{2}\dot{r}_{H_2O_2} \quad [\text{mol/m}^2\text{s}] \qquad (7\text{-}14)$$

It is common to assume for the kinetic constant, k'', a temperature dependency through the so-called Arrhenius exponential form, parametrized with the *activation energy E_a* [J/mol] and *pre-exponential factor*

A_s [m/s]. The former is a property of the catalytic material; the latter is more dependent on the specific integration and deposition process of the catalyst over the support.

Note that k'' is perhaps the most important parameter dictating the effectiveness of the catalytic decomposition within the dissociation chamber (the highest the better). In the numerical analysis, it will be assumed as an independent parameter in the simulations: clearly one must choose reasonable values within a certain range. However, it is not possible to know a-priori the "true" value k'', that one will encounter during experimental activities, since it depends on many factors such as the nature of the chosen catalyst material, but also the technological process used for the deposition of the catalyst on the pillars' surface.

The kinetic experiments performed at our Lab on two commercial granular catalysts showed that in the range of temperature 23 - 50°C the activation energy is in the order of 50 kJ/mol, which is consistent with available literature data. A direct application of the kinetic constant experimentally determined is questionable, since, as said above, it is dependent on the way the catalytic material is integrated, nevertheless this is a good reference point.

Much of literature data reports the kinetic constant on a volumetric [1/s] basis (more useful for homogeneous catalysis), rather than a surface [m/s] basis, as it is required by the FEM code implementation. The few available reporting pre-exponential factor in m/s are quite spread in the range of 10^3 to 10^6 m/s, yielding to k'' in the range $[10^{-4} - 10^{-1}]$ m/s for temperatures up to ≈ 430 K; these values are expected to increase further if vaporization completes and fluid temperature grows beyond such value. An extensive compilation of literature data can be found in [5] and references therein.

For the simulations presented here, values of k'' were drawn from the above range, however, a simplifying assumption has been made. Since the Arrhenius exponential dependency was found to prevent convergence of the numerical solver, we chose to model the reaction kinetics assuming *independency* over the temperature. This way, when drawing considerations starting from the results of the *simulations* we should regard the prescribed constant k'' as an "average" value of the kinetic constant to be achieved under experimental conditions across the reactor length in the estimated temperature range.

Note that this strong assumption it is actually justified for the present study: as will be apparent when analyzing the simulation results, the presence of the highly conductive silicon substrate limits the fluid temperature jump between the beginning end the end of the catalytic pattern to few tens of degrees. Therefore, only relatively small variations of the kinetic constant are expected due to temperature variation.

7.4 Solid domain

The energy equation in the solid domain (silicon pillars and substrate) reads as:

$$\rho c_p \frac{\partial T}{\partial t} = \nabla \cdot (\kappa \nabla T) + Q \qquad (7\text{-}15)$$

Where Q [W/m^3] is any heat source placed inside the material, such as due to joule heating, which is applicable in case of a resistive element placed in the substrate. The fluid and solid domain are coupled by means of energy exchange through the common boundaries by prescribing the same temperature at the interface (i.e. no solid-fluid temperature slip): this feature is handled automatically by the FEM software.

DISTRIBUTION A. Approved for public release: distribution unlimited.

The exterior solid boundaries are assumed to be coupled with the surrounding ambient through natural convection, by letting:

$$q = H_{nc}(T_a - T) \ [\text{W}/m^2]$$
(7-16)

With T_a = 298K and H_{nc} = 40 W/m^2 is a value representative of natural convection through air.

7.5 Set-up for the simulations

Simulations have been performed with an inlet mass flux of 0.1 mg/s. Outlet pressure is at atmospheric condition. Note that, since only one elementary pattern of the staggered pillars has been simulated, to get an indication of the actual mass flow through the whole device one should multiply by the total number of pillars rows and accounting, at the same time, for the momentum losses due to the chamber lateral walls. Overall, one should expect the design mass flow rate of the combustion chamber being a fraction of the CFD single-row mass flow multiplied by the number of pillars rows.

Several attempts were made to enhance convergence: as a matter of fact, the formidably coupled system of equations which create the whole numerical model pose quite a challenge to the converge of the solution.

The parameters used for the baseline test case are summarized in **Table 7-3**.

Three modes for running the simulations were considered:

1- Steady state simulations using a *continuation* technique for the $k^{''}$ parameter. This consists of multiple steady state simulations run at increasingly higher values of $k^{''}$ (called a continuation parameter) spanning from extremely low values (10^{-7}) up to $1 \cdot 10^{-3}$ m/s. The solution for each value of $k^{''}$ was then used as initial guess for the next iteration of the continuation loop.

2- Transient simulations with a constant value of $k^{''}$ and initial conditions taken from a previously converged solutions at lower $k^{''}$. These tests were done basically in an attempt to enhance convergence of the solutions.

3- Transient simulations; a smooth profile was assigned to the $k^{''}$ parameter up to its regime value. These tests give an indication of a start-up phase of the device.

In general, steady state simulations were achieved only up to a value of k'' = 2e-3; to simulate higher kinetic rates, it was then mandatory to switch to *transient simulations*, whether using approach 2 or 3. These, however, increased the computational burden even more.

Despite many "tuning" efforts to enhance convergence of the simulations, to date reaching complete evaporation within one simulation was not possible, due to errors encountered by the solver. Nevertheless, a very good insight could be achieved by the simulations, which allowed to simulate the evaporation within the dissociation chamber to a degree higher than 90%.

7.5.1 Summary of Boundary Conditions and main parameters setting

In the following table, a summary of the BC's applied to the domain for the different physics are collected

Boundary	Boundary Condition	Equation
Mass Balance		
Inlet	Mass fraction	$Y_i = Y_{i0}$
Outlet	No diffusive flux	$-\mathbf{n} \cdot \rho D_i^m \nabla Y_i = 0$
Reactor walls	Prescribed total flux	$-\mathbf{n} \cdot \rho(D_i^m \nabla Y_i + \mathbf{u} Y_i) = \dot{r}_i M_i$
Bottom walls	Null total flux	$-\mathbf{n} \cdot \rho(D_i^m \nabla Y_i + \mathbf{u} Y_i) = 0$
Symmetry walls	Null total flux	$-\mathbf{n} \cdot \rho(D_i^m \nabla Y_i + \mathbf{u} Y_i) = 0$
Momentum Balance		
Inlet	Mass flow rate	$-\int_{\partial\Omega} \rho \, (\mathbf{n} \cdot \mathbf{u}) dS = \dot{m}$
Outlet	Pressure	$-p\boldsymbol{I} + \mu(\nabla\mathbf{u} + \nabla\mathbf{u}^T) - \frac{2}{3}\mu(\nabla \cdot \mathbf{u}) = -p_0$
Reactor Walls	No slip	$\mathbf{u} = \mathbf{0}$
Bottom Walls	No slip	$\mathbf{u} = \mathbf{0}$
Symmetry walls	Symmetry	$\mathbf{n} \cdot \mathbf{u} = \mathbf{0}$
Energy Balance, Fluid domain		
Inlet	Interface with isothermal domain at T=T$_o$	$\mathbf{n} \cdot k\nabla T = \rho u_x [H(T_o) - H(T)]$
Outlet	No conductive flux	$\mathbf{n} \cdot k\nabla T = 0$
Reactor walls	Boundary Heat Source	$\mathbf{n} \cdot k\nabla T = Q_{reac}$
Symmetry walls	No conductive flux	$\mathbf{n} \cdot k\nabla T = 0$
Energy Balance, Solid domain		
Reactor walls	Temperature continuity with fluid	T=T$_{fl}$
External walls	Convective flux	$\mathbf{n} \cdot k\nabla T = H_{nat}(T_{ext} - T)$
Symmetry walls	No conductive flux	$\mathbf{n} \cdot k\nabla T = 0$

Table 7-2: Summary of boundary conditions for the CFD decomposition chamber analysis

Symbol	Value [units]	Description
k''	from 1e-7 to 5e-3 [m/s]	Average kinetic constant
$\dot{m}$	1e-7 [kg/s]	Inlet mass flow rate
D_i^m	1e-6 [m/s]	Mixture average diffusion coefficient (common to all species)
δ_p	1e-4 [m]	Pillars spacing (channel width)
H_{nat}	40 [W/(m²K)]	Coefficient of natural convection heat transfer
P_J	0 [W]	Heat supply by joule effect
T_{PC}	398.15 [K]	Assumed phase change temperature
ΔT	50 [K]	Assumed width of phase change T interval

Table 7-3: Summary of baseline test cased parameters considered for the CFD decomposition chamber analysis

7.6 Results

7.6.1 Numerical consistency of the solution

It is known that Finite Element methods do not exactly solve the conservation equations within the domain, but only approximately. Therefore, it is useful to address to which extent, on a global domain scale, the conservation equations are satisfied. To this end, the following two tests have been set up which focus on the mass and energy conservation:

$$\iint_{A_{in}} \rho u_x Y_{H_2O_2} dA_{in} - \iint_{A_{out}} \rho u_x Y_{H_2O_2} dA_{out} = \iint_{A_{cat}} \dot{r}_{H_2O_2} M_{H_2O_2} dA_{cat} \tag{7-17}$$

$$P_{out} = P_{in} \rightarrow \iint_{A_{out}} \rho u_x H(T_{out}) dA_{out} + \iint_{A_{in}} \rho u_x [H(T_{in}) - H(T_o)] dA_{in}$$
$$+ \iint_{A_{ext}} H_{nat}(T_{ext} - T) dA_{ext} = \iint_{A_{in}} \rho u_x H(T_{in}) dA_{in} + \iint_{A_{cat}} Q_{reac} dA_{cat} \tag{7-18}$$

which are applicable only for simulations at steady state.

The first equation above dictates that the difference of the outgoing peroxide mass flux to the ingoing flux must equate the peroxide mass flux reacting at the catalytic surfaces (A_{cat}). This condition also automatically guarantees that the enthalpy of reaction is consistent with the degree of conversion predicted by the simulation. The second equation requires that the energy entering the computational domain (i.e. enthalpy of the inlet stream plus heat of reaction) equates the energy leaving the system through three mechanisms. These are: 1) the enthalpy of the outlet stream, 2) the losses through external silicon surfaces towards the ambient, and 3) as the enthalpy lost to heat up the propellant from its isothermal reservoir condition at T_o up to the computed T_{in} at the inlet.

In all steady-state simulations, the above equality was satisfied with an accuracy within $\approx 1\%$.

7.6.2 Flow topology

Flow results are presented here through a series of 3D plots of the relevant flow properties: velocity, density, temperature, hydrogen peroxide mass fraction, evaporation fraction. Plots are shown for values of $k^{''}$ = [1e-4, 1e-3, 4.5e-3] m/s. Apart from the first value for which a direct steady state solution was feasible, the remaining test cases were in MODE#2: the plots shown correspond to the last time step.

In the following, some considerations emerging from inspection of pictures in Figure 7-4, Figure 7-5 and Figure 7-6 are briefly listed:

- Velocity and Reynolds number are increasing considerably on the streamwise direction: this is a direct consequence of the decreasing mixture density spanning three orders of magnitude from $\approx 10^3$ down to 10^0 kg/m^3.
- Pressure drop across the pillars modelled chamber length is on the order of 3-4 kPa.
- Temperature variations across the pillars are quite limited, when compared to the predictions made using simplified 1D models based on plug-flow theory. This is due to the presence of a highly conductive silicon substrate, which makes any analysis neglecting the fluid-solid conjugate heat transfer problem hardly applicable.

- For the same reason, we can notice that the vaporization is quite well spread across the reactor length, and not concentrated in a thin region.
- By looking at the plots of the peroxide mass fraction, one notice that higher decomposition is found close to the reacting pillars, which is to be expected since the reaction is not volumetric but a surface phenomenon. As a matter of fact, a strong role is played by mass diffusivity (D_k^m), due to the lack of turbulent flow mixing inherent to the low-Re micro-scale regime.
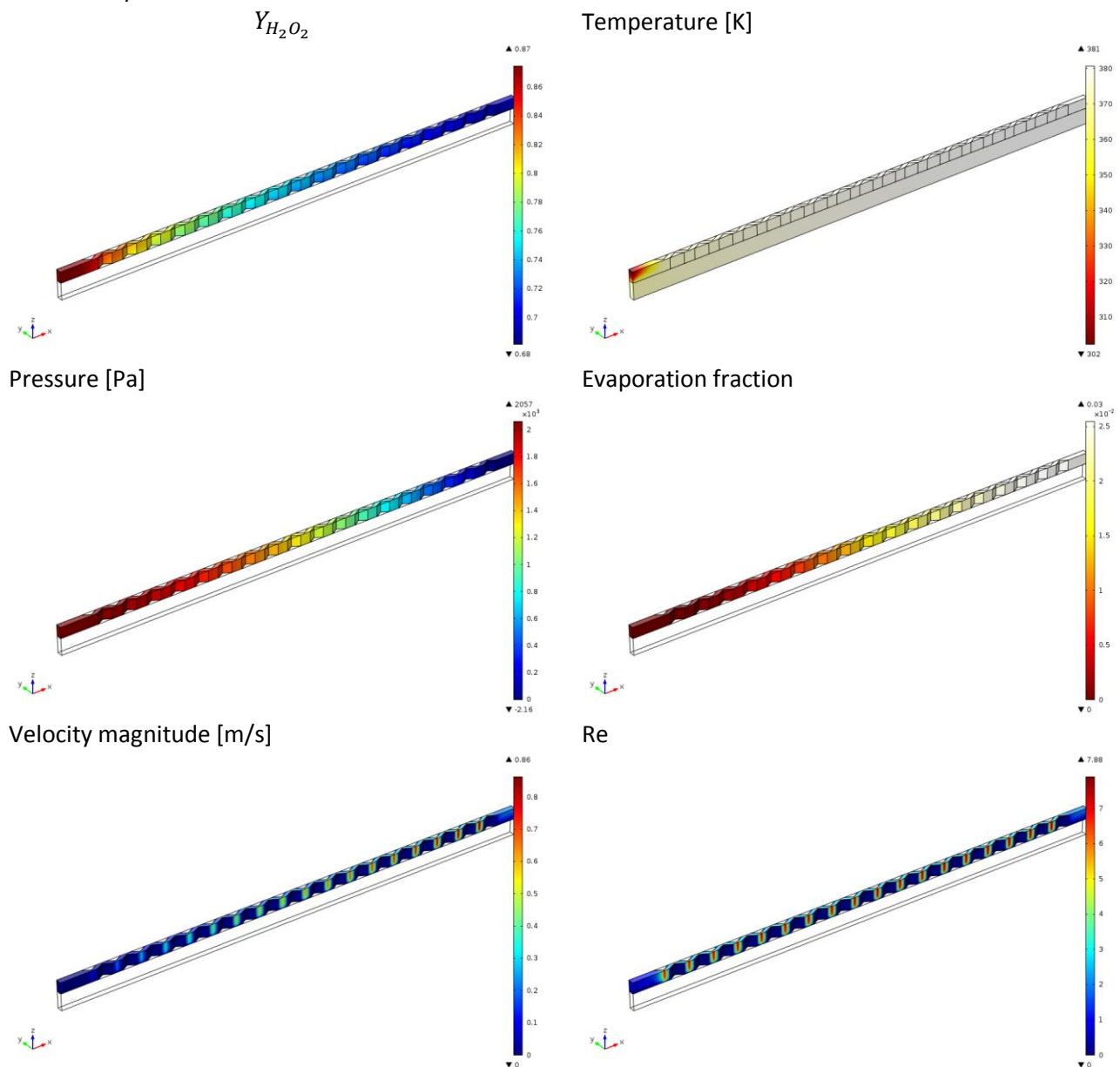
k'' = 1e-4 m/s

$Y_{H_2O_2}$ Temperature [K]

Pressure [Pa]   Evaporation fraction

Velocity magnitude [m/s]   Re

Figure 7-4: Plots of relevant fluid and solid properties, k'' = 1e-4 m/s

k'' = 1e-3 m/s

$Y_{H_2O_2}$ Temperature [K]

DISTRIBUTION A. Approved for public release: distribution unlimited.

Pressure [Pa]

Evaporation fraction

Velocity magnitude [m/s]

Re
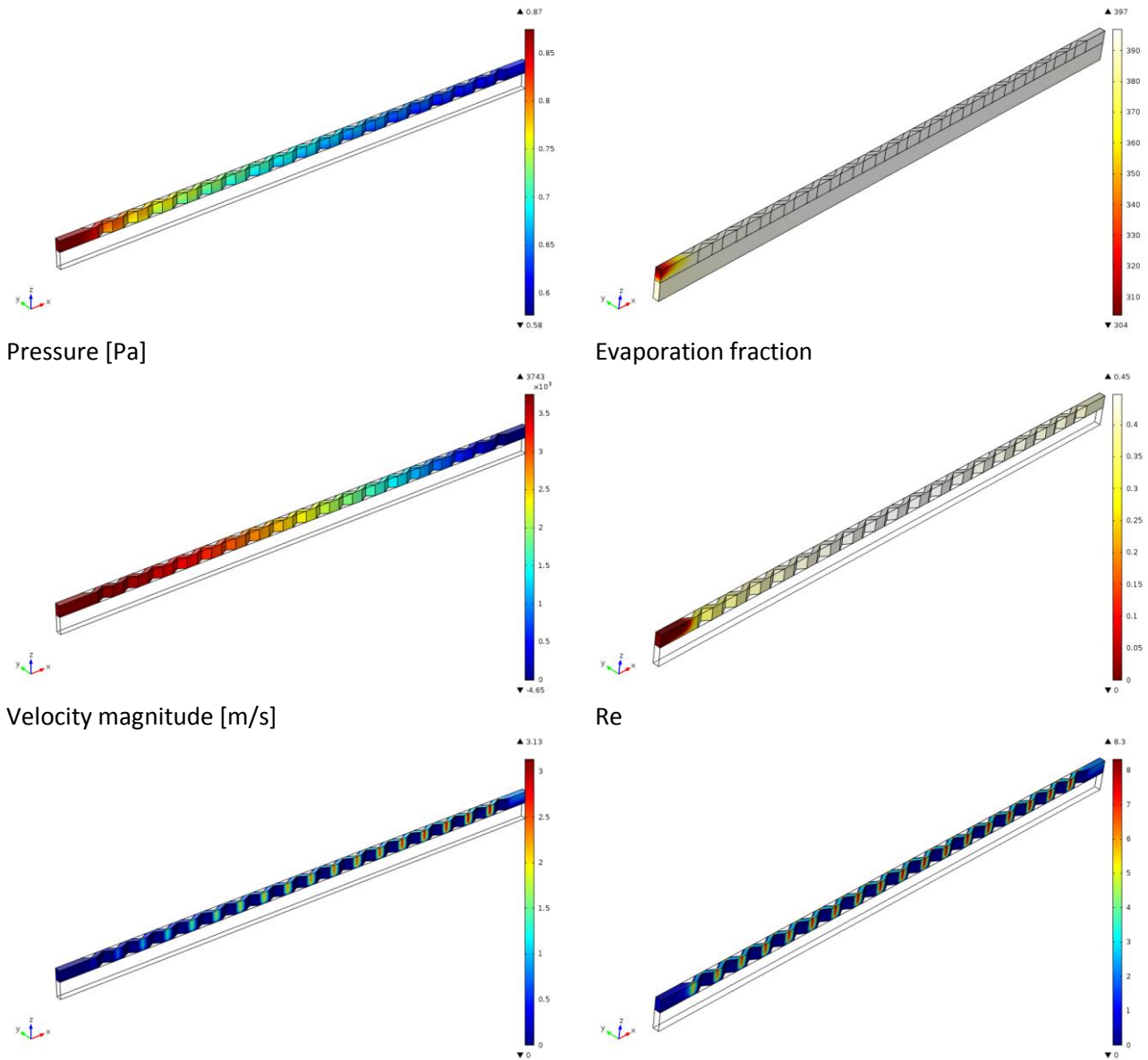
Figure 7-5: Plots of relevant fluid and solid properties, k'' = 1e-3 m/s
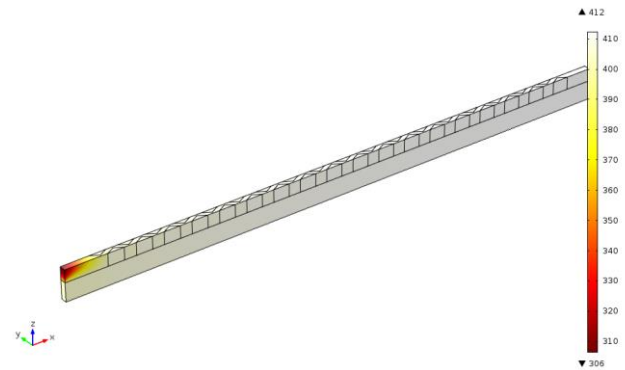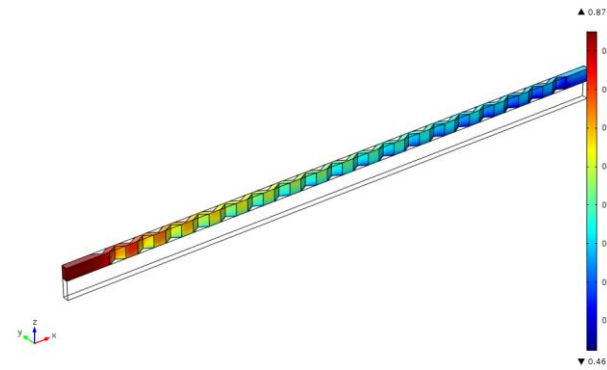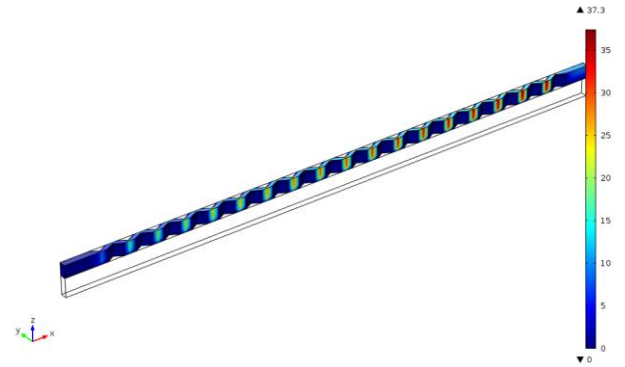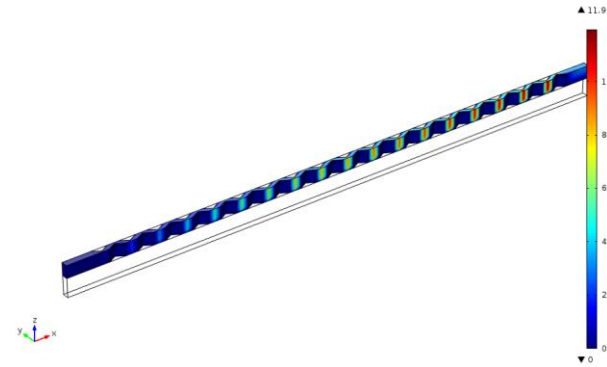
$k^{''}$ = 5e-3 m/s

Figure 7-6: Plots of relevant fluid and solid properties, k'' = 4.5e-3 m/s

Figure 7-7: Sample close-up views of the peroxide mass fraction (left) and stramwise velocity (right)

7.6.3 Combustion chamber performance

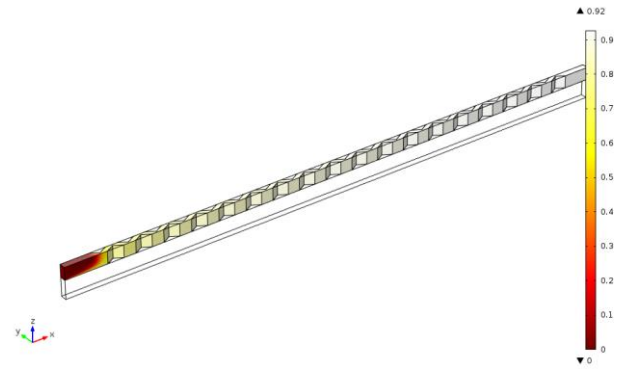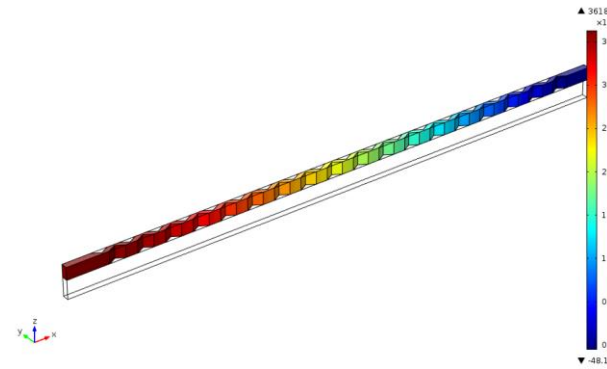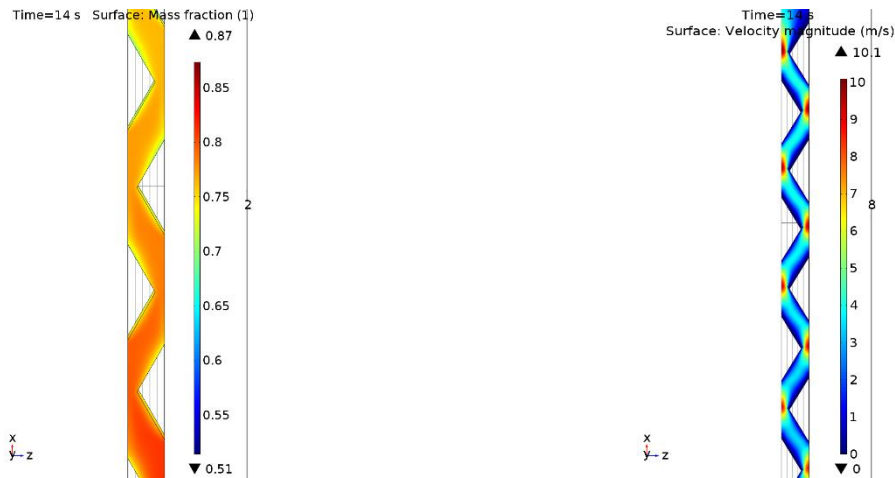To evaluate the performance of the combustion chamber, we focus onto relevant fluid properties averaged at the outlet surface, such as propellant percentage conversion[4], temperature and vaporization fraction. Results will be reported for Mode#3 simulations: overall, this set-up, was the one allowing to get to a result with the lowest solution time. The highest value of k'' reaching convergence were between $4.2 \cdot 10^{-3}$ and $4.5 \cdot 10^{-3}$ m/s. Attempts to get beyond those values resulted into solver errors.

. Different settling time for the kinetic constant raising phase have been used to explore possible differences in the transient phases, when using steeper or smoother transients.

These quantities are collected for the various simulations in the tables below. For other relevant parameter values employed for the simulations, refer to **Table 7-2**, **Table 7-3**.

Settling Time for k'': 14 s				
Kinetic constant k_s'' [m/s]	Outlet peroxide mass fraction [-]	Propellant conversion [%]	Temperature [K]	Evaporation fraction [%]
1e-3	0.67	22	405	73
4.5e-3	0.58	34	412	92

Table 7-4: Results of the simulations for different values of the kinetic constant, diamond pillars, uniform spacing.

7.6.4 Effect of change in pillars base geometry

The effect of a changing the pillars' base geometry was preliminary addressed, by testing a square base, in opposition to the diamond baseline configuration. The side of the square base was chosen as to maintain an equal Surface/Volume (S/V) ratio, i.e. $l_x=l_y$=0.140 mm, according to the nomenclature of **Table 7-1**. The spacing between adjacent pillars was also kept fixed. Results are summarized in **Table 7-5**

---

[4] Defined as $\left(Y_{H_2O_{2-\text{in}}} - Y_{H_2O_{2-\text{out}}}\right)/Y_{H_2O_{2-\text{in}}} \cdot 100$.

Settling Time for k'': 12 s				
Kinetic constant k_s'' [m/s]	Outlet peroxide mass fraction [-]	Propellant conversion [%]	Temperature [K]	Evaporation fraction [%]
1e-3	0.67	23	405	74
4.2e-3	0.58	34	412	92

Table 7-5: Results of the simulations for different values of the kinetic constant, square pillars, uniform spacing.

7.6.5 Effect of variable pillars' spacing

The effect of variable spacing of the pillars was also addressed. In particular, a negative gradient along the streamwise direction has been explored: the rationale for this is that it might be convenient to have higher S/V ratios when the propellant concentration is low, and lower S/V when concentration is high, in order to have a more uniform reaction rate[5] along the chamber. The geometry simulated started from an initial spacing which was doubled that of the baseline geometry at the inlet, which decreases linearly the baseline value at the outlet.

Settling Time for k'': 6 s				
Kinetic constant k_s'' [m/s]	Outlet peroxide mass fraction [-]	Propellant conversion [%]	Temperature [K]	Evaporation fraction [%]
1e-3	0.56	36	364	0
4.5e-3	0.59	33	411	91

Table 7-6: Results of the simulations for different values of the kinetic constant, diamond pillars, variable spacing.

Settling Time for k'': 12 s				
Kinetic constant k_s'' [m/s]	Outlet peroxide mass fraction [-]	Propellant conversion [%]	Temperature [K]	Evaporation fraction [%]
1e-3	0.67	23	404	72
4.2e-3	0.59	33	411	91

Table 7-7: Results of the simulations for different values of the kinetic constant, square pillars, variable spacing.

In general, the effects of changes in geometry and pillar spacing are rather negligible.

7.6.6 Transient response of the device: thermal-chemical coupling

The successful operation of the device relies on its capability of producing a hot gaseous stream at its outlet.

---

[5] Reaction rate is approximately proportional to the product $S/V \cdot C_{H_2O_2}$

**DISTRIBUTION A. Approved for public release: distribution unlimited.**
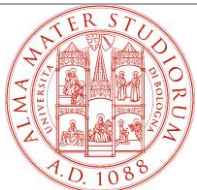
This in turn does not depends *solely* on the complete decomposition of the peroxide, but also on a careful thermal management of the device itself. It is clear that there is competition between the heat generated inside the device and the heat losses through the silicon walls towards the ambient. The ratio of heat losses (a surface phenomenon) to heat of reaction (a volumetric quantity) increases, as the device is downscaled, with the inverse of the characteristic dimension. Furthermore, due to the *high thermal conductivity* of the silicon substrate, heat transport does not act only on the transversal (towards ambient) direction, but has also a significant component on the *stream-wise direction*. This means that a plug-fow 1-D analysis may fail considerably in predicting the outlet flow conditions, since the usual assumption of a vaporization process taking place in a thin spatial region is no more applicable. Therefore, also the fluid vaporization will somehow tend to move upstream.

On one side, this can be thought as a beneficial effect since it enhances vaporization. On the other side, since a considerable fraction of hydrogen peroxide vaporize before decomposing, the propellant concentration decreases (due to the lower mixture density), which results, according to the assumed 1st order reaction kinetics, to a substantially reduced rate of decomposition. Furthermore, a drawback may arise due to the fact that the mixture density decreases as a result of vaporization, and its average speed increases. This may turn the reactor towards a diffusion limited operation mode (too high *u/D*) which basically means that the peroxide flow is convected away from the reaction pillars too fast, before having the chance to decompose completely.

A practical view of the above phenomenon is seen by looking at the temporal evolution of the outlet decomposition in the example below. dealing with a transient simulation performed at $k'' = 4.5e\text{-}3$ m/s, starting from a converged solution obtained at $k'' = 1e\text{-}3$ m/s (i.e. a Mode#2 simulation). Three pictures are shown, depicting the evolution of the average outlet a) *peroxide concentration*, b) *vaporization fraction* and c) *temperature* in the first 0.35 seconds of simulation (temporal resolution is 0.05 s).
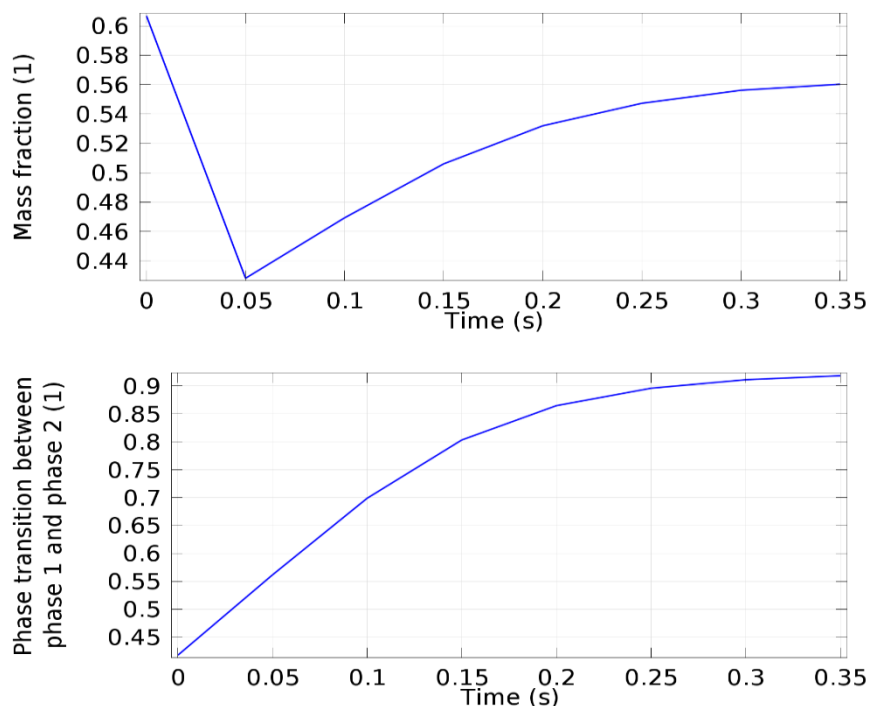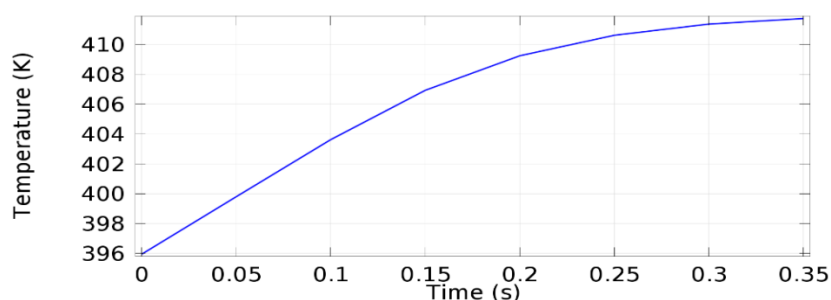
Figure 7-8: Average outlet evolution of mass fraction (top), evaporation fraction (middle) and temperature (bottom).

The first picture is representative of the strong coupling between thermal effects and reaction kinetics: at the first time step the outlet peroxide fraction decreases strongly from the equilibrium value of 0.6 for a $k^{''}$ = 1e-3 m/s (the initial condition) down to 0.44 due to the enhanced kinetic $k^{''}$ = 4.5e-3 m/s. At subsequent times, the trend is reversed, with the outlet $Y_{H_2O_2}$ increasing due to the reduced peroxide concentration, which is in turn a direct consequence of the ongoing evaporation (mixture density decreasing).

On one side, we see the expected behavior for both the temperature and vaporization fraction, which increase monotonically. On the other side, the degree of conversion at the outlet is only marginally higher than the one obtained at the lower $k^{''}$.

A similar behavior was encountered also with analysis run in Mode#3, for sufficiently short raising times of the kinetic constant (**Table 7-6**). As an example, in Figure 7-9 results are shown obtained with a simulation where $k^{''}$ was allowed to raise from 1e-7 to 4.5e-3 m/s in 6 seconds. Again, while the temperature raises steadily, the outlet concentration does not decrease in a monotonic way, with a bump occurring when the fluid is evaporating.

These results suggest that it is unlikely that a complete decomposition will be reached unless much higher temperatures are achieved through other means (externally supply through e.g. joule heating). This later conclusion however, shall be further investigated, and definitive conclusions can be drawn once a full simulation up to complete evaporation will be achieved.

Finally, it is worth to be noted that, when increasing the settling time for the kinetic constant up to 12-14 s (as per **Table 7-4**, **Table 7-5** and **Table 7-7**), the propellant conversion follows instead a monotonic decrease.

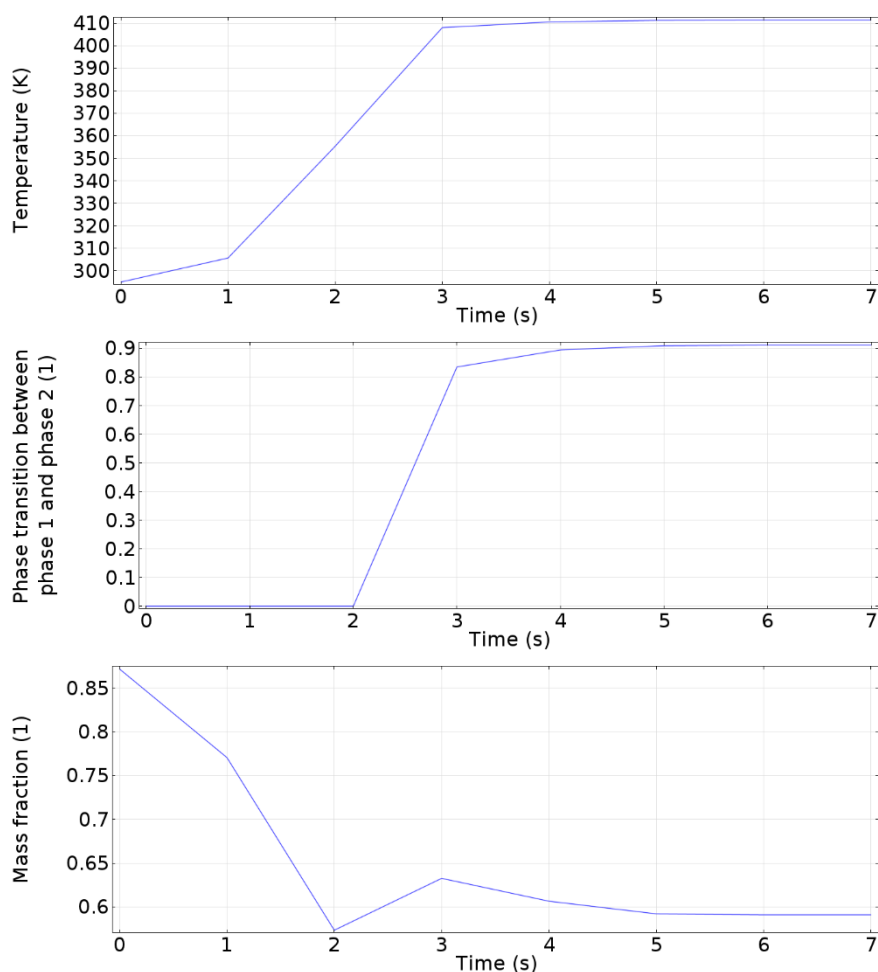**DISTRIBUTION A. Approved for public release: distribution unlimited.**
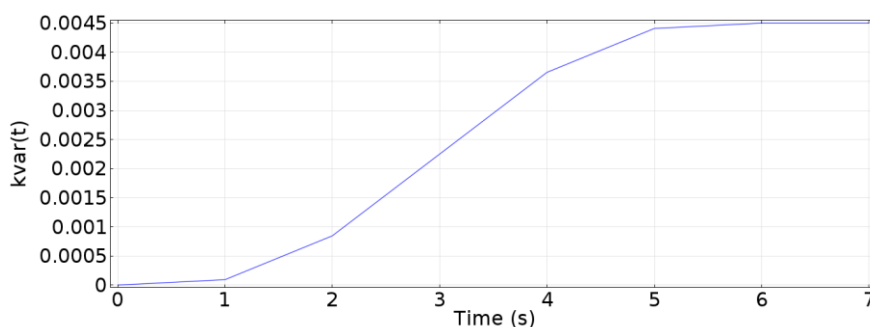
Figure 7-9: Prescribed kinetic constant (top panel) vs temperature, evaporation fraction, and outlet peroxide concentration obtained with a Mode#3 simulation.

7.6.7 Post vaporization phase

Since complete vaporization was not reached with a single simulation, a separated treatment of the post vaporization phase has been set up: this consisted in using the same geometry, but feeding as inlet a gaseous stream with a temperature equal to 150°C (i.e. the top end of the vaporization interval) and a peroxide mass fraction extrapolated from previous results. In average, the highest degree of vaporization was achieved for a peroxide concentration of 59%, which was taken as input for the present simulations. With this single-phase setup, convergence was easily achieved with steady state simulations.

As a further investigation, we checked the effect of the change in order of magnitude of the diffusivity coefficient, whose baseline value 10^{-6} m^2/s, is quite high for the gaseous phase. In the table below, the results of this test for the square diamond are summarized, for values of the kinetic constant k'' taken as 10^{-2} and 10^{-1} m/s.

Diffusivity coeff. [m²/s]	Kinetic constant k_s'' [m/s]	Outlet peroxide mass fraction [-]	Propellant conversion [%]	Temperature [K]
1e-8	1e-2	0.42	52	436
	1e-1	0.15	83	463
1e-7	1e-2	0.42	52	436
	1e-1	0.14	84	464
1e-6	1e-2	0.36	54	437
	1e-1	0.10	89	464

Table 7-8: Results for the post-vaporization simulations

The degree of propellant conversion at the outlet lies in between 83% and 89%, with the highest value achieved when diffusion coefficient is set at a maximum, as expected.

7.6.8 Summary

The results of the post-vaporization suggest that a length on the order of the entire modeled domain is needed to obtain an almost complete decomposition, or even larger as the diffusivity reduces. One could then be tempted to assume an overall length being twice the nominal length: one to achieve full evaporation, and one to achieve full decomposition within the gaseous phase. This would lead, however, to an overestimation, since only by simulating at once from liquid inlet to vapor outlet we can model consistently the thermal coupling of the substrate.

7.7 A step forward in the FEM analysis

We know that the decomposition of the propellant starts as soon as the hydrogen peroxide gets in contact with the catalyst. The initial temperature is usually well below the boiling point such that the formed water is in the liquid phase. The oxygen is in the gas phase and it appears as bubbles in the liquid. Since the reaction is exothermic, the generated heat causes a rise in temperature until the boiling point of the liquid mixture is reached. The increase in temperature also leads to an increase in the reaction rate leading to more gas bubbles in the liquid. Some bubbles will coalesce with other bubbles forming larger bubbles or slugs. Together with the liquid water, part of the peroxide evaporates before it can decompose in the liquid phase leading to even more gas. At this point, rather than speaking about a liquid phase with gas bubbles dispersed in it, it makes more sense to speak about a gas phase with liquid droplets dispersed in it. Eventually, all of the liquid has vanished either by decomposition or evaporation. Gaseous peroxide will decompose as resulting in a further increase in gas temperature. What remains is a gas mixture of steam and oxygen.

Clearly, all the features above cannot be captured by the FEM model described previously, which relies on the homogeneous fluid assumption: an advancement in the level of detail of the FEM analysis can be pursued, which accounts for the coexistence within the dissociation chamber of liquid and gas as separated phases. The first steps towards such development is outlined in the following.

DISTRIBUTION A. Approved for public release: distribution unlimited.

7.7.1 Modelling Non-homogeneous multiphase flow with phase change

The development of a complete computational model that takes into account the entire decomposition process is extremely challenging. Chemical and thermal point of view aside, treatment of the multiphase flow component during the initial stages of the decomposition is especially difficult and, at the same time, the literature is very limited.

In this section, we report the groundwork for an upcoming, comprehensive approach to the multiphasic modelling of the problem. The first step is the assessment of a numerical model for describing phase change in the proximity of a solid domain. This is representative of the catalytic decomposition at the pillar where, other than the chemical reaction, a change of phase occurs (from liquid peroxide to gaseous oxygen).

COMSOL Multiphysics, offers several physics interface to simulate different kind of multiphase flow problems, therefore initially an assessment was performed to select the most suitable for the present investigation. Given our focus and in particular, the need to capture the movements of the fluid interface and of incorporate subsequently COMSOL physical nodes, as the chemical reaction and thermal ones, we opted for the *Two-Phase Level Set Interface*. This physics interface solves the Navier-Stokes equations (conservation of momentum) and a continuity equation (conservation of mass), according to:

$$\rho \frac{D\mathbf{u}}{Dt} = \nabla \cdot [-p\boldsymbol{I} + \mu(\nabla\mathbf{u} + \nabla\mathbf{u}^T)] + \boldsymbol{F_g} + \boldsymbol{F_{st}}$$
$$\nabla \cdot \mathbf{u} = 0$$

(7-19)

Where **u** is the velocity field, p the pressure field, μ the dynamic viscosity of the mixture, $\boldsymbol{F_g}$ the gravity force and $\boldsymbol{F_{st}}$ the surface tension force acting on the interface between the two fluids.

The interface position is tracked by solving a transport equation for the level set function:

$$\frac{\partial \phi}{\partial t} + \mathbf{u}\nabla \cdot \phi = \gamma\nabla \cdot \left(\varepsilon\nabla\phi - \phi(1-\phi)\frac{\nabla\phi}{|\nabla\phi|}\right)$$

(7-20)

The left-hand side represent interface advection, while the right-hand side term includes stabilization and reinitialization terms. In particular, ε controls the interface thickness and parameter γ defines the intensity of γ is the *reinitialization parameter* (set to 1 by default), ϕ is the *level set function* (set to 0.5 at the interface) and ε is the *interface thickness controlling parameter* (set as default to $h_{max}/2$ where h_{max} is the maximum element size in the component). The level set function is fundamental to define the boundary between the immiscible phases, which assumed to be located at $\phi = 0.5$. In the future, the level set function will be used to set specific regions in the domain where interface phenomena occur, such as evaporation.

The main objective is to model the production of the gas phase at the catalytic surface. For this purpose, a solid theoretical base arrives from studies related to phase change phenomena [7] . They are very useful, in our case, for two reasons:

- We can approximate the production of oxygen as a phase change in a small region around the surface of the pillars;
- We can model the evaporation of water and peroxide due the exothermic chemical reaction.

DISTRIBUTION A. Approved for public release: distribution unlimited.

The governing equations involved to simulate an isothermal, laminar and incompressible two-phase flow with a phase change are essential the default relations, seen previously, with the addition of some source terms both in the continuity and in the level set transport equations:

$$\nabla \cdot \mathbf{u} = \dot{m}\left[\frac{1}{\rho_v} - \frac{1}{\rho_l}\right] \tag{7-21}$$

$$\frac{\partial \phi}{\partial t} + \nabla \cdot (\mathbf{u}\phi) = \gamma \nabla \cdot \left(\varepsilon \nabla \phi - \phi(1-\phi)\frac{\nabla \phi}{|\nabla \phi|}\right) - \frac{\dot{m}}{\rho_l} \tag{7-22}$$

where $\dot{m}$ is the rate of phase change, ρ_l and ρ_v are the density of the liquid and gas phase, respectively. The source terms have been implemented in COMSOL Multiphysics as weak contributions.

This method models the change of phase as a volume phenomenon, while ideally, we would like it to happen as a boundary one, i.e. occurring at the reactive surface. This drawback was overcome by confining the source terms within a small volume surrounding the pillar (see Figure 7-11).

Finally we underline also that the use of the conservative form in Eq. (7-22) was found to be of paramount importance to ensure mass conservation: by using conservative form, the level set function assumes the meaning of volume fraction, rather than that of an advected physical boundary, as in Eq. (7-20).

7.7.2 A mass conservation test

To validate the implemented model a simple conservation test was set up. The purpose of which is to verify that:

- the amount of gas generated is consistent with the prescribed rate of production $\dot{m}$;
- the mass of gas generated corresponds to the mass of liquid consumed due to phase change.

To this end, we considered a simplified domain with a single diamond pillar (Figure 7-10). Apart from the *outlet* on the right, all the boundaries are considered as *wall* with *no-slip* condition. As *initial value*, the blue region represents the liquid domain while the red region represents the gas domain; the latter is included to avoid that liquid phase getting out of the domain, therefore ensuring that liquid phase disappears only due to phase change.
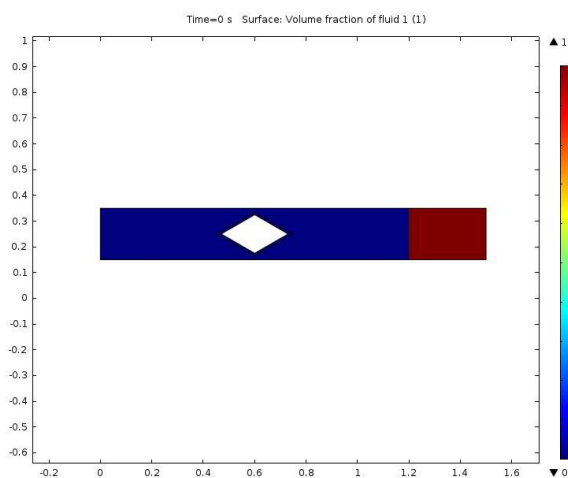

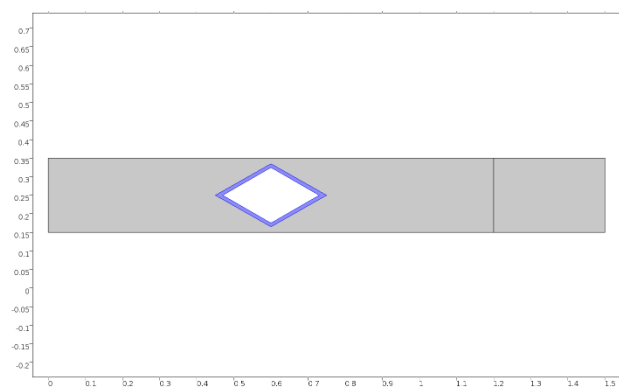**Figure 7-10: Volume fraction of gas at time 0s**

Figure 7-11: Geometric domain with highlighted the region where gas phase creation occurs

Results are shown in the following, in particular:

- Figure 7-12 that the mass of gas produced during time (blue line) reaches the theoretical value prescribed by the chosen source $\dot{m}$ (green line);
- Figure 7-13 shows that, parallel to gas production, an equal amount of liquid phase exits the domain.

As stated also at the end of the previous section, the mass conservation is not satisfied when implementing interface advection in non-conservative form.
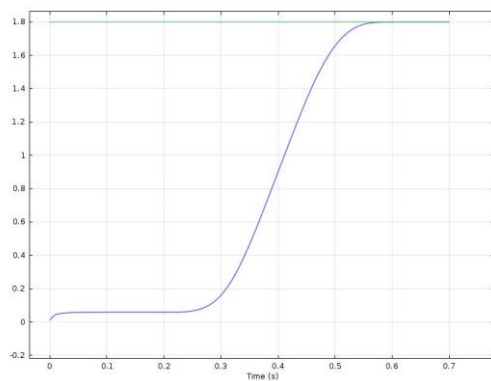

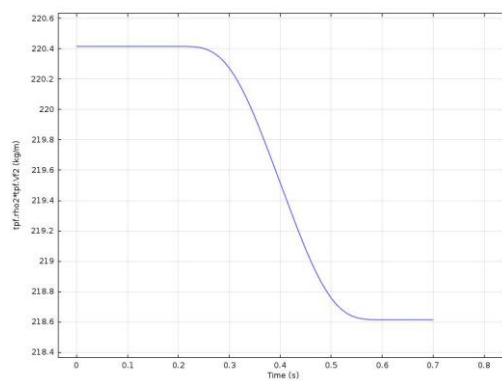**Figure 7-12: Mass of gas included in the domain**
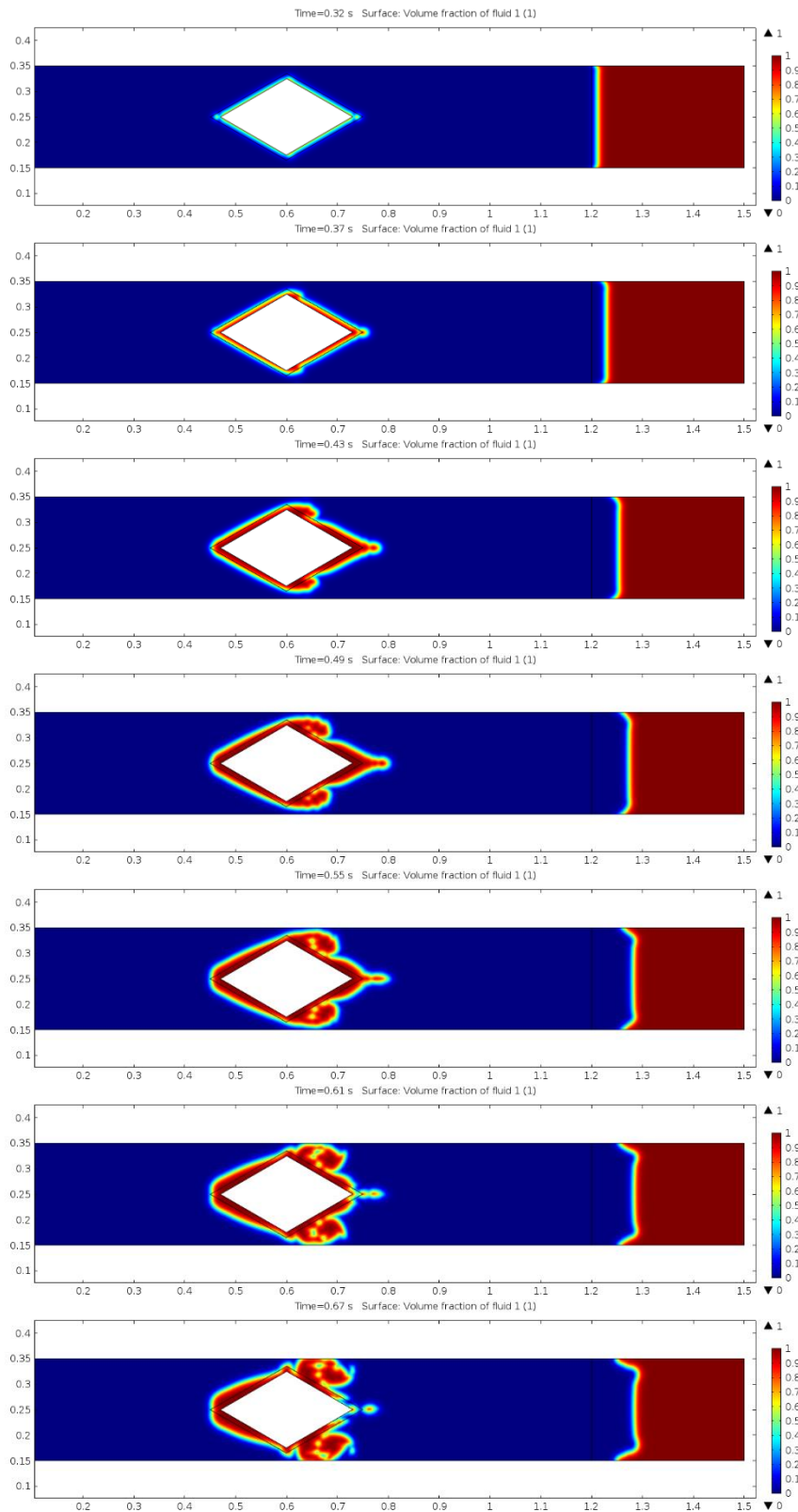

Figure 7-13: Mass of liquid included in the domain

Figure 7-14: Snapshots of the temporal evolution of gaseous phase created at the pillar during the mass conservation test.

DISTRIBUTION A. Approved for public release: distribution unlimited.

8. MICROTHRUSTER DESIGN

The numerical analysis performed so far provided some good insight into the physical mechanisms governing the decomposition of the propellant. Nevertheless, quantitative guidelines for an optimal design of the chamber cannot be drawn with enough confidence such to select a priori a single preferred design for prototyping.

Furthermore, manufacturing constraints needs to be considered: for example, despite one would like having the catalytic surfaces as close as possible (i.e. low pillar spacing), on the other side, this would result in decreased accessibility of the pillars lateral surface when it comes to catalyst deposition. Catalyst, whether platinum or palladium, is deposited through PVD process using an e-gun in a vacuum chamber equipped with a planetary sample holder undergoing a "wobbling" rotational motion. The uniformity of the deposition is difficult to be addressed quantitatively: this can be done, partially, only *a-posteriori*, by cutting the devices and inspecting the resulting sections with a scanning electron microscope.

For this reasons, for the design of the next generation of prototypes an approach was chosen which tries to explore a design space as much as possible: the main design parameters are the length, width, shape/size of the pillars and spacing. This approach is made possible since the manufacturing process (DRIE, deep reactive ion etching), allows to accommodate tens of devices within a single process: etching on a 6'' diameter, 625 µm thick silicon wafers.

Two pillars geometry were considered: diamond and arrow-like, and for each of them 3 different widths, 2 lengths and whether uniform or variable spacing pillars have been designed. This results in a total of 24 geometries which are due for production. A sample drawing for one of this geometry is shown in Figure 8-1.
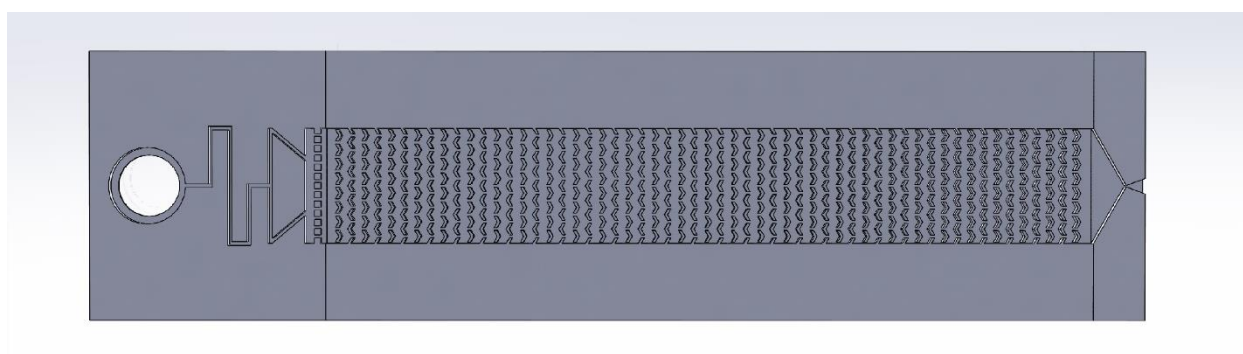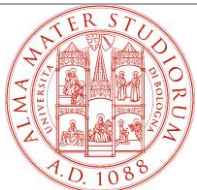

Figure 8-1: Example of 1 out of 24 thruster geometries due for manufacturing.

8.1 Design of a test bench for the microthruster

Testing of microfluidic devices is quite a complex task, and often the design of an ad-hoc test bench is mandatory for an efficient handing of the experimental activities.

The microthruster is essentially composed by an inlet region with a circular hole at the base, a decomposition chamber and an exit region with a convergent/divergent nozzle. At the base of the central region, characterized by a series of catalytic pillars, there are applied a series of electrical resistances with two purposes: heating this region to enhance the rate of reaction; measuring the temperature as resistance

thermometer. Accordingly, the test bench (Figure 8-2) must enable both a fluid dynamic connection, for the propellant feeding, and an electrical connection for the wiring system.
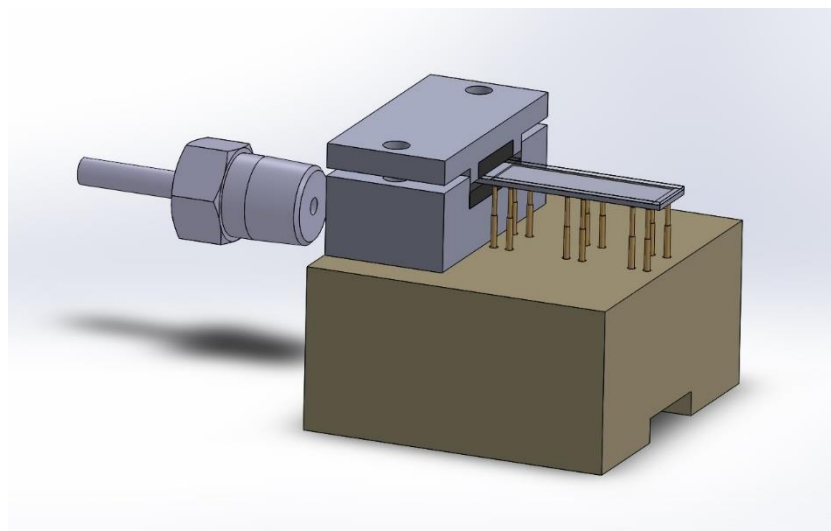

Figure 8-2: Concept for the test bench

For the preliminary design of a test bench there are some problems:

- Centering of the device;
- Leakage at the inlet;
- Coupling between the fluid dynamic connection and the electrical one.

The concept, analyzed in this section, tries to solve these issues with a solution that is reliable, practical and flexible for different size of microthrusters.

About the first point, considering the flexibility feature of the system, it is necessary to center the device through the inlet by a cylindrical component (Figure 8-3).
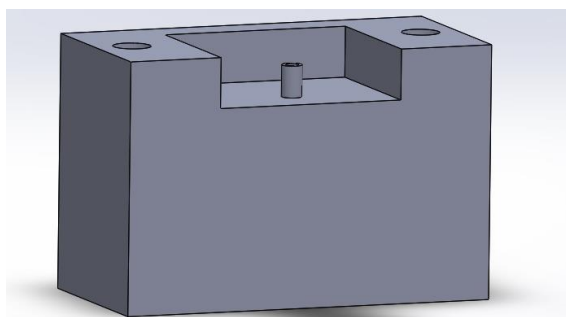

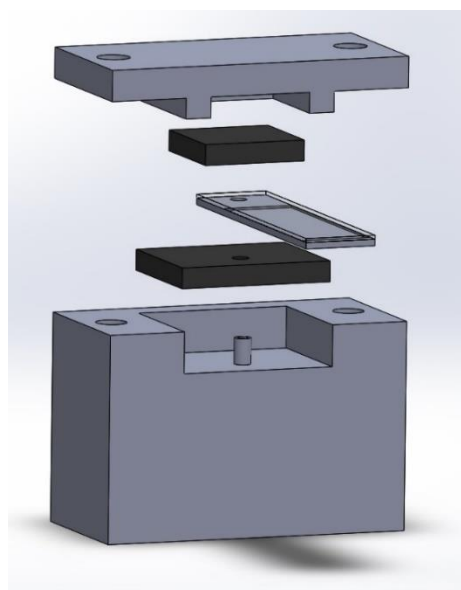**Figure 8-3 Lower part of the fluid dynamic connection**

Figure 8-4: Exploded diagram of the fluid dynamic connection

DISTRIBUTION A. Approved for public release: distribution unlimited.

The seal at the entry hole of the propellant is guaranteed by two gaskets (Figure 8-4), pressed against the thruster through a bolt-nut system.

The electrical connection, is essentially realized through a series of spring contact probes. For this to work it is fundamental using a non-conductive material and an accurate centering to ensure an effective contact between the probes and the heating/sensing elements.

9. CONCLUSIONS

This report discusses the activities performed under USAF AFOSR Grant n° FA9550-16-1-0081. These have been part of a wider collaboration of the team within a consortium for the development of HTP MEMS-based micro-thrusters in the mN range thrust.

The most relevant contribution is the development of a numerical model which jointly simulates the chemical, fluid-dynamics and thermal behavior of the propellant stream inside the combustion chamber, as well as the thermal coupling with the silicon substrate. Within this model, an element of novelty is represented by the inclusion of the evaporation equations based on the variable heat capacity method and the concept of pseudo-phase. This method, offers a tractable, yet consistent, way to model the evaporation in a chemical reacting mixture. As a main result of the analysis, it emerged that the silicon substrate has a great impact on the flow evolution, such that the evaporation region is distributed all over the length of the device. Transient simulations allowed to get more insight into the coupling of thermal and chemical related phenomena, showing a non-monotone degree of conversion at the outlet due to the decrease of the propellant density.

A sensitivity study was performed to insect the impact of variable geometry and non-equispaced pillars. Overall, the impact on the degree of conversion achieved at the outlet was found to be quite low.

A strategy was also outlined for increasing further the level of detail of the simulation with a non-homogeneous multi-phase analysis, based on a modification of the level-set method to allow for the change of phase at the catalytic surface. The consistency of the approach has been validated through mass conservation tests, with good results. Addition of chemical reactions and thermal equations is till to be performed. The high computational burden suggests that such method hardly could be extended to include a fully coupled multiphysics simulation on a 3D domain: most likely, this approach will rather be confined to more fundamental research objectives, such as validation of the homogeneous model in a simplified, lower dimensional test case.

Some design activities were also performed in preparation of the manufacturing of the next batch of prototypes. With respect to the previous ones, these will incorporate actuators and sensors in the form of heating elements and resistive temperature sensors. Different combustion chambers were designed, with equispaced or variable spaced pillars.

Since the past experience with the previous prototypes showed that the interfaces are a critical part of the system design, a dedicated mounting support has been designed which will allow both fluidic and electrical reliable connections.

The batch of prototypes are due to production at an external research institution in the next weeks. Results of both the experimental activities and of the numerical ones will be published on the open literature, with the due acknowledgement of the funding source.